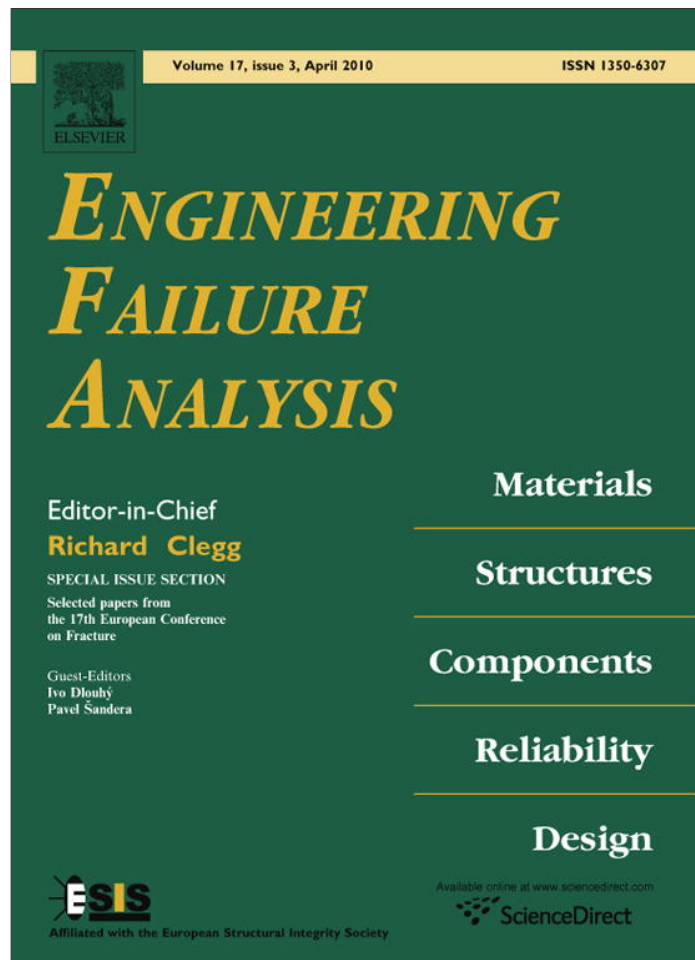


Provided for non-commercial research and education use.
Not for reproduction, distribution or commercial use.

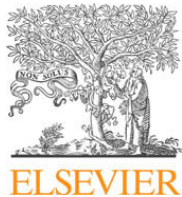


This article appeared in a journal published by Elsevier. The attached copy is furnished to the author for internal non-commercial research and education use, including for instruction at the authors institution and sharing with colleagues.

Other uses, including reproduction and distribution, or selling or licensing copies, or posting to personal, institutional or third party websites are prohibited.

In most cases authors are permitted to post their version of the article (e.g. in Word or Tex form) to their personal website or institutional repository. Authors requiring further information regarding Elsevier's archiving and manuscript policies are encouraged to visit:

<http://www.elsevier.com/copyright>



Contents lists available at ScienceDirect

Engineering Failure Analysis

journal homepage: www.elsevier.com/locate/engfailanal

Quasistatic fracture behaviour and defect assessment of brazed soft martensitic stainless steel joints

Christian Leinenbach^{a,*}, Hans-Jakob Schindler^b, Tanya A. Başer^a, Niklaus Rüttimann^c, Konrad Wegener^c

^aEMPA-Swiss Federal Laboratories for Materials Testing and Research, Laboratory of Joining and Interface Technology, Dübendorf, Switzerland

^bMat-Tec AG, Winterthur, Switzerland

^cETH Zürich, Institute of Machine Tools and Manufacturing, Zürich, Switzerland

ARTICLE INFO

Article history:

Received 12 December 2008

Received in revised form 12 May 2009

Accepted 13 May 2009

Available online 19 May 2009

Keywords:

Brazing

Fracture toughness

Defect assessment

Failure assessment diagram

ABSTRACT

Brazed components are widely applied in industry and are often subjected to complex loading conditions. Even if such components often contain brazing defects, no failure assessment procedures for brazed joints are reported in the literature. In this work, the deformation and the quasistatic behaviour of brazed joints of the martensitic stainless steel X3CrNiMo13-4 were investigated. This includes the determination of stress–strain–curves as well as of the fracture toughness. In addition, the mechanical behaviour of components such as specimens with T-joint geometry under tensile loading were characterized. In order to consider the effect of brazing defects on the structural integrity, typical defects with different sizes and geometries were introduced in the brazing zone. The experimentally determined material parameters were used for additional numerical deformation analyses by means of finite elements (FE). Both the experimental and the numerical results were in good agreement with predictions according to the R6 method and provided a basis for the engineering defect assessment of brazed components based on failure assessment diagrams.

© 2009 Elsevier Ltd. All rights reserved.

1. Introduction

High temperature (HT) furnace brazing is widely applied in industry as a quick and cost-effective method for joining large components used in the aerospace and the chemical industry as well as for power generation, e.g. compressor impellers or turbine parts [1–3]. These components are subjected to complex loading conditions in service, comprising mechanical, thermal or thermo-mechanical loads. As such, they can be classified as class A joints according to the American National Standard AWS C3.6 M/C3.6:2008, which are subjected to special safety requirements [4].

Brazed joints form a heterogeneous anisotropic system consisting of a base material, a diffusion zone and a filler metal. The mechanical properties of brazed joints are not only determined by those of the individual materials, but in a more complex way through various interactions. The main parameters influencing the overall properties are the joint geometry, the gap width, the microstructure as well as the size and the distribution of defects. It is known that in thin interlayer metals joined to the base metals with different elastic–plastic properties, a triaxial stress state is produced under tensile loading due to the mechanical constraints, restricting the transverse contraction of the interlayer and making the deformation behaviour more complex [5,6]. The triaxial stress state reduces the effective or von-Mises-stress. This usually results in higher strengths of brazed components in comparison to the filler metal's strength determined on bulk specimens [7].

* Corresponding author. Tel.: +41 44 823 4518; fax: +41 44 823 4039.
E-mail address: christian.leinenbach@empa.ch (C. Leinenbach).

During brazing, defects such as pores or incomplete gap filling may arise and act as stress concentrations, leading to crack growth and spontaneous failure. Fig. 1 shows as an example a void as a result of incomplete gap filling in a steel joint brazed with a silver based filler metal. According to [4], voids with a maximum size of 2.3 mm with a total accumulated length of less than 10% of the fillet length would be acceptable for class A joints. However, this recommendation does neither take into account the specimen geometry nor the loading conditions and it is not specified how this value was derived. Thus, defect assessment of brazed components is of practical interest in order to determine the critical size of a defect for a given loading condition.

In applied fracture mechanics, the influence of material defects on the structural integrity is often estimated with failure assessment diagrams (FAD). In the FAD approach, which is used in several failure assessment procedures such as R6 [8], BS7910 [9] or SINTAP [10], two dimensionless parameters, L_r and K_r , are calculated, as

$$L_r = \frac{F}{F_Y} \quad (1a)$$

and

$$K_r = \frac{K_I}{K_{Ic}} \quad (1b)$$

where the first parameter describes the structure's resistance against plastic collapse, F is the actually applied load and F_Y the yield load of the defect containing structure. K_r describes the resistance against fracture, where K_I is the stress intensity at the defect and K_{Ic} is the fracture toughness. Having calculated both parameters, the point (L_r, K_r) is plotted on an FAD, and failure is avoided provided that:

$$K_r \leq f(L_r) \quad (2)$$

Various forms of the function $f(L_r)$ have been determined semi-empirically by mathematical simulation of different component and failure geometries as well as experimental testing. The most widely used form of $f(L_r)$ is R6/option 3 [8], which is defined by

$$f(L_r) = \left(1 + 0.5L_r^2\right)^{-0.5} \left[0.3 + 0.7 \exp\left(-0.6L_r^6\right)\right] \quad (3)$$

While the applicability of this approach has been demonstrated for defect containing bulk materials or welded components no information on the feasibility of the above mentioned defect assessment procedures on brazed components can be found [11].

The aim of the present work was to study the feasibility of the commonly applied R6 method for a defect assessment of brazed components. Therefore, the quasistatic deformation and fracture behaviour of HT brazed specimens of the soft martensitic stainless steel X3CrNiMo13-4 and the filler metal Au-18Ni was investigated firstly in order to determine the required material parameters. Then, the mechanical performance of component-like tensile specimens with a T-joint geometry containing artificial defects was characterized. The quasistatic fracture behaviour of the brazed steel joints was investigated by stereomicroscopy and scanning electron microscopy (SEM) on fractured specimens. The experimentally obtained material parameters were used for additional numerical stress and strain analyses of the T-joint specimens by finite element (FE) methods. Finally the results were compared with predictions according to the R6 method.

2. Materials and testing procedures

2.1. Materials and brazing process

In this work, the soft martensitic stainless steel X3CrNiMo13-4, which is widely applied in the chemical industry and in power generation, was used as base material. Foils of the binary alloy Au-18Ni with a thickness of 100 μm were applied as

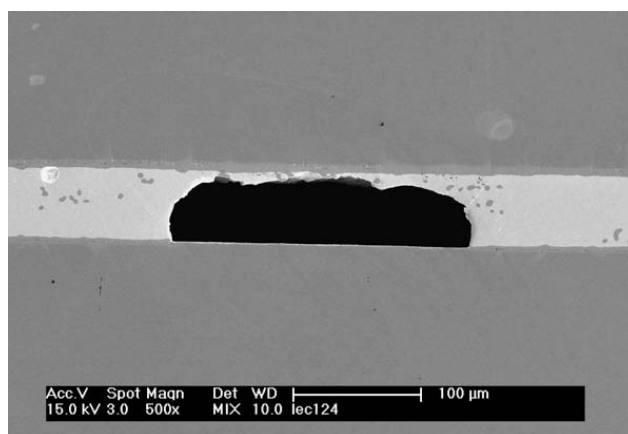


Fig. 1. SE-micrograph showing a void as a result of incomplete gap filling in the brazing zone of a steel joint brazed with an Ag-based filler metal.

filler metal. Cuboidal steel plates with the dimensions of $300 \times 100 \times 25$ mm were brazed using a special brazing jig. Brazing was performed in an industrial shielding gas furnace (SOLO Profitherm 600) at a temperature of 1020°C for 20 min. As shielding gas, Hydro-Argon 7 (93 vol.% Ar, 7 vol.% H_2) was used. The addition of hydrogen to the argon allows removing the oxide film from the stainless steel surface, which is essential for filler metal wetting. After brazing, the specimens were tempered at 520°C for 5.5 h in nitrogen atmosphere. At the end of this process, a homogenous braze joint with a brazing zone width of approximately $100\ \mu\text{m}$ was obtained.

2.2. Strength and fracture behaviour

In order to determine the mechanical properties of the steel joints, standard round tensile specimens with a diameter of 10 mm and a gauge length of 50 mm as well as tubular specimens with an outer diameter of 16 mm and an inner diameter of 12 mm for quasi-static torsion tests were manufactured from the brazed steel plates. The fracture behaviour under quasi-static loading was investigated using double cantilever beam (DCB) specimens with the dimensions $B \times 2h \times t = 90 \times 60 \times 8$ mm. A sketch of the DCB specimens is shown in Fig. 2. For all specimen types, the brazing zone was positioned in the middle of the samples. After machining of the DCB specimens a notch with a total length of 35 mm was introduced into the brazing zone by electro discharge machining (EDM) using a wire with a diameter of 0.3 mm.

Tensile tests were performed on a standard electro-mechanical testing machine (Schenck Trebel RSA 250 kN) with a deformation velocity of $10\ \text{mm min}^{-1}$. Torsion tests were performed on a biaxial servo-hydraulic testing machine (Schenck Hydropuls PTT S59). The axial load was held constantly at 0 kN and the torsion rate was set to $0.05\ \text{s}^{-1}$. The ultimate shear stress τ_{max} can be calculated from the maximum measured torque at fracture as $\tau_{\text{max}} = M_{\text{max}}/W_p$, where $W_p = 5.5 \times 10^{-7}\ \text{m}^3$ denotes the section modulus for the given geometry.

The quasi-static fracture behaviour was characterized on the same electro-mechanical testing machine as the tensile tests. Therefore, a special holder for the DCB specimens was mounted, allowing an initial load introduction perpendicular to the braze layer. The deformation velocity was set to $1.6\ \text{mm min}^{-1}$. The fracture toughness for mode I loading was determined from load-displacement curves. The crack mouth opening displacement (CMOD) was measured with a clip gauge positioned on the side plane where the starter notch was introduced. The stress intensity K_I and the CMOD as functions of the specimen geometry and the applied load, respectively, were derived in [12] and can be written as:

$$K_I = \frac{F}{Bh^{0.5}} \left(8 + 13.25 \frac{a}{h} + 12 \left(\frac{a}{h} \right)^2 \right)^{0.5} \tag{4a}$$

$$\text{CMOD} = \frac{2F}{BE} \left(\frac{8a + 8d}{h} + \frac{6.624a^2 + 13.25ad}{h^2} + \frac{4a^3 + 12da^2}{h^3} \right) \tag{4b}$$

where F is the applied force, B and h are the specimen geometry as described above, a is the total crack length measured from the load initiation point, d is the distance between the load initiation point and the specimen edge and E is the Young's modulus.

2.3. Mechanical properties of the filler metal

The elastic–plastic material properties of the Au–18Ni filler metal are important for FE simulations of the deformation behaviour of brazed joints. However, these parameters cannot be easily evaluated from the above mentioned tensile and

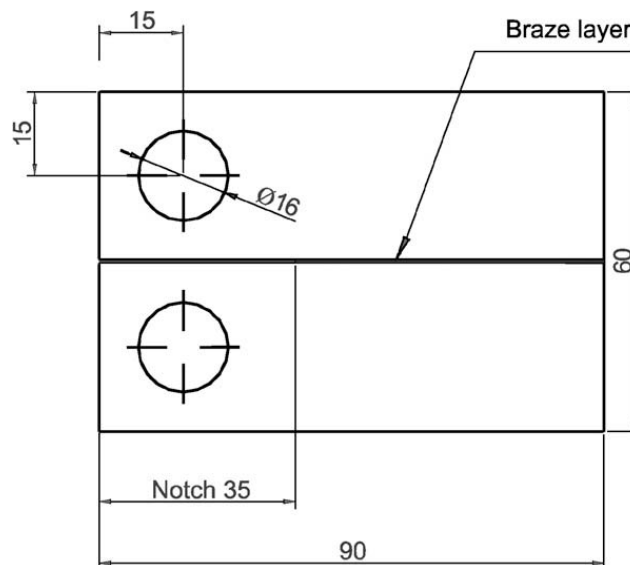


Fig. 2. Geometry of DCB test specimens.

torsion tests. Moreover, tensile or torsion tests with cast standard specimens of Au–18Ni would be extremely cost intensive. It can be expected that the microstructure of a cast specimen would differ completely from the microstructure of the relatively thin braze layer, thus leading to different mechanical parameters.

In order to determine the stress–strain-curve of the filler metal more precisely, in situ tensile tests inside a SEM were performed. Miniaturized dog bone shaped tensile specimens with a width of 5 mm and a thickness of 1.5 mm (cf. Fig. 3) were clamped in a special testing device (Kammrath & Weiss) and tested at a constant deformation velocity of $0.5 \mu\text{m s}^{-1}$ to fracture. The test was interrupted at certain load levels and a sequence of high quality micrographs as a function of the applied load were taken.

On the digital images, two correlation grids with 9×1 cells were positioned along the interfaces between the steel and the filler metal (cf. Fig. 4a). The relative displacement of characteristic features inside the marker zones was detected by digital image correlation, using a correlation algorithm developed at EPF Lausanne [13]. Fig. 4b shows an SEM image of the specimen prior to fracture at a stress of 950 MPa. The arrows indicate the reference points which were used to determine the displacement during loading. The applied stress–strain curve of the filler metal was derived from the load–displacement curves by averaging eight individual measurements.

The uniaxial stress–strain curve was determined by comparing the experimental results with the results of additional FE calculations. A 3D model of the tensile specimen including the brazing zone was created using the commercial FE Code AnsysTM, taking specimen symmetries into account. The stress–strain behaviour of the steel joints was assumed to follow Hooke's law in the elastic range and the plastic part according to Eq. (5):

$$\sigma_y = k \cdot (\varepsilon_{yp} + \varepsilon_p)^n \quad (5)$$

where σ_y is the yield stress, k is the hardening coefficient, ε_{yp} is the elastic strain at the beginning of plastic flow, ε_p is the logarithmic plastic von-Mises strain and n is the hardening exponent. The elastic parameters for the steel and the filler metal (i.e. $E_{\text{steel}} = 210 \text{ GPa}$, $\nu_{\text{steel}} = 0.30$, $E_{\text{Au-18Ni}} = 100 \text{ GPa}$, $\nu_{\text{Au-18Ni}} = 0.42$) were taken from literature. Initial values for the yield stress, the 0.2% proof stress, the ultimate tensile stress and the elongation to fracture were estimated according to the results of the tensile and torsion tests. The material parameters of the filler metal were then optimized in iterative FE calculations.

2.4. Tensile testing of specimens with T-joint geometry

To investigate the influence of brazing defects on brazed components experimentally, tensile tests with special T-joint specimens were performed (cf. Fig. 5a). After machining of the specimens, crack-like defects of different geometries (i.e. straight and semi-elliptical) and sizes were introduced into the brazing zone by EDM. With this, typical brazing defects arising from incomplete gap filling should be simulated. Fig. 5b shows a sketch of the artificial brazing defects. Straight defects with a size of $a = 2 \text{ mm}$ and $a = 4 \text{ mm}$ were tested (defect A + B). For the semi-elliptical defects (defect C), a ratio of $a/c = 2/3$ with $a = 3 \text{ mm}$ was chosen. The results of tensile tests on defect-free specimens served as a reference. At least two tests per specimen type were performed with the tensile testing machine described above with a deformation velocity of 0.01 mm s^{-1} . Selected fractured specimens were investigated using a stereo microscope (Zeiss Stemi SV11) and a scanning electron microscope (Philips-FEG XL3).

3. Numerical simulation of tensile tests with T-joint geometry

The tensile tests on T-joint specimens were additionally simulated by FE methods. The aim was to numerically determine the critical limit loads. A 3D model of the complex joint geometries was created with the FE code AnsysTM taking specimen symmetries into account. Ideal bonding between the steel and the filler metal was assumed. A mesh of hexalateral brick elements with eight nodes (SOLID164) was created. In the brazing zone, the element size was set to 0.05 mm, whereas the element size in the base material was set to 0.5 mm. The mesh size was chosen as an optimum between the accuracy of the simulated load–displacement response of the joint and the FE solution time. The model was then transferred to the FE code LS-DYNATM, which was used for any further calculations as well as for data post processing. The deformation behaviour was described by an elastic–plastic deformation law, with Hooke's law describing the elastic part and plastic part according to Eq.

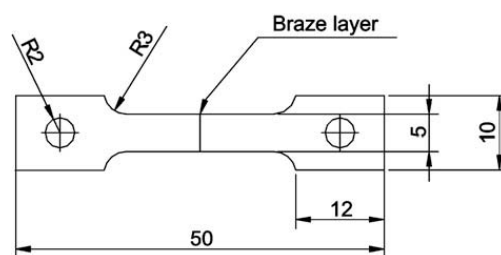


Fig. 3. Geometry of miniaturized dog bone specimen.

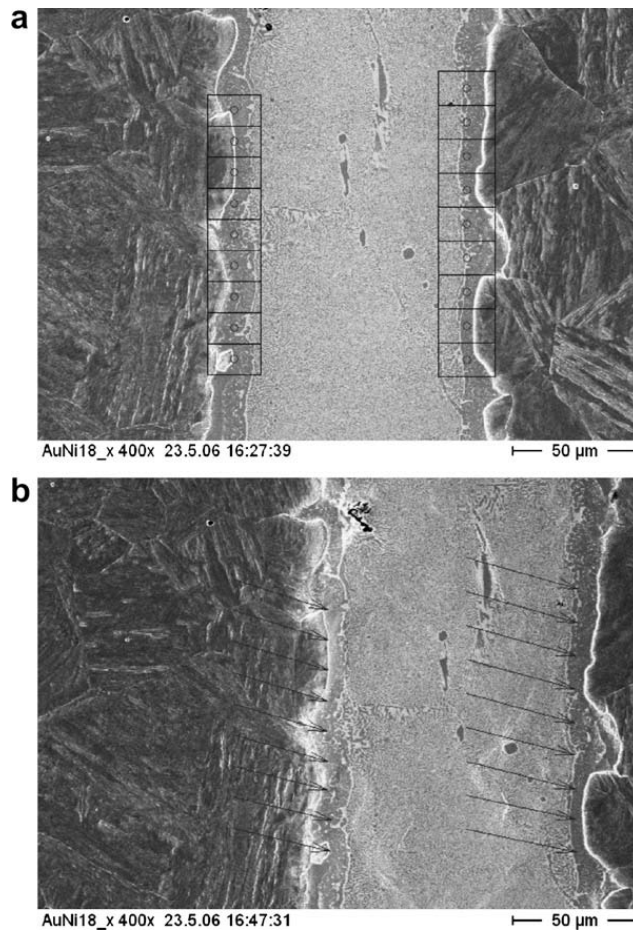


Fig. 4. SE-micrograph of miniaturized tensile specimen with correlation grids: (a) before in situ tensile test, (b) at a stress of 950 MPa, \leftrightarrow loading direction.

(3). The material parameters were taken from the stress–strain determined as described in Section 2.4. In order to prevent hourglass phenomena at large deformations as well as necking, a Belytschko-Bindemann integration scheme was used [14]. The specimen was defined to fail when the von-Mises-strain exceeded the fracture strain according to Table 1 in the region of

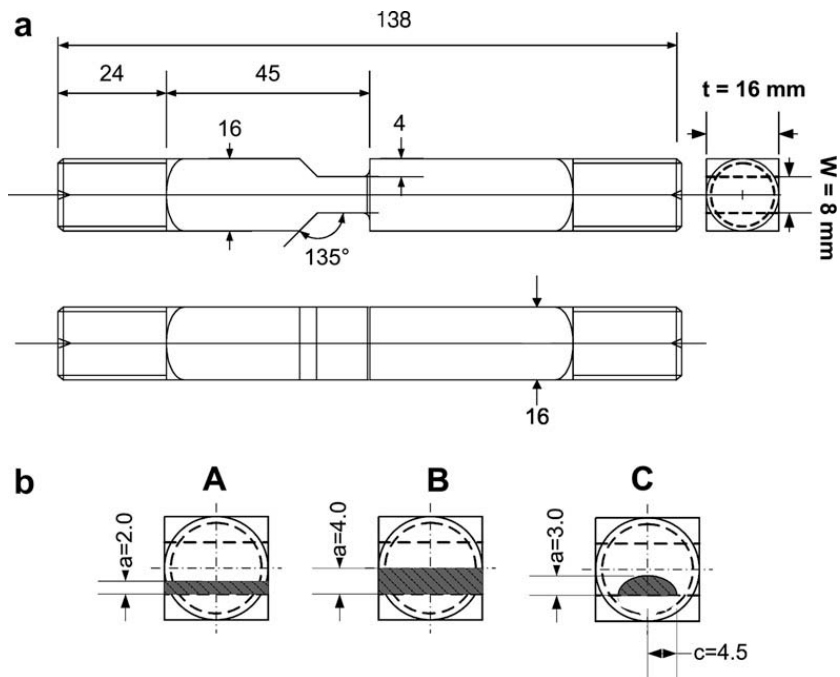


Fig. 5. (a) Geometry of T-joint tensile specimens; (b) defect geometries of straight (A, B) and semi-elliptical (C) defects.

the highest deformation. With the corresponding stress the stress intensity at the defect edge was calculated. It was found that on the defined specimen failure the stress intensity reached values of approximately K_{Ic} .

In Fig. 6a the meshed specimen and the resulting von-Mises stresses of a specimen with a semi-elliptical defect subjected to tensile loading are presented. Fig. 6b shows the stress distribution in the vicinity of the defect. For a better visibility, the upper part of the T-joint specimen was removed from the picture. As expected, the stress maxima are located at the edges of the defect.

4. Results and discussion

4.1. Strength and fracture behaviour

In Fig. 7, the uniaxial stress–strain curves for the steel as determined in standard tensile and for the Au–18Ni filler metal as determined in the in situ tensile tests described in Section 2.4 are presented. In Table 1, the mechanical properties of the base material, the filler and of the braze joint are summarized. The results for the steel and for the brazed joint are average

Table 1
Mechanical properties of X3CrNiMo13-4, X3CrNiMo13-4–Au–18Ni braze joints and Au–18Ni.

	0.2% proof strength (MPa)	Ultimate tensile strength (MPa)	Elongation to fracture (%)	Torsion yield strength (MPa)	Ultimate torsion strength (MPa)
X3CrNiMo13-4	920 (±5)	975 (±25)	17.5 (±2.5)	620 (±5)	660 (±10)
X3CrNiMo13-4–Au–18Ni joint	923 (±7)	976 (±15)	6 (±0.5)	245 (±10)	539 (±7)
Au–18Ni	555	940	6.5	–	–

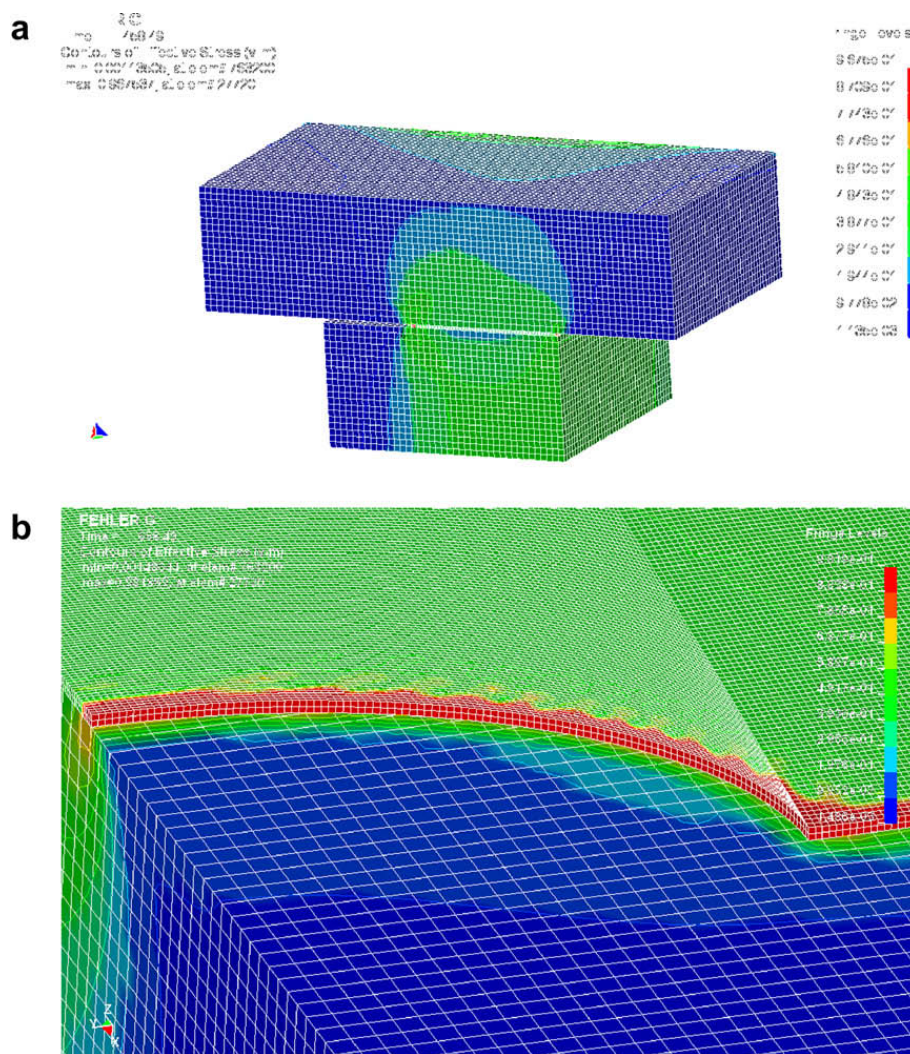


Fig. 6. FE model of T-joint tensile specimen (a), distribution of von-Mises-stresses in the vicinity of a semi-elliptical defect (b).

values over 3–4 tensile or torsion tests. All specimens fractured in the brazing zone. Brazed specimens showed nearly the same yield and tensile strength as the base material, whereas significant differences were detected under torsion loading. This is a result of the pronounced constraining effect that the surrounding base material imposes on the thin braze layer, which prevents the latter from yielding as long as the former remains essentially elastic [4,5]. In a first approximation, the yield and the tensile strength of the filler metal can be estimated by the von-Mises-criterion to about twice the corresponding values for torsion loading, the torsion yield strength and the ultimate torsion strength, respectively (cf. Table 1). This behaviour was confirmed in the in situ tensile tests and the inverse numerical simulations. In Fig. 7 it can be seen as well that the yield strength of the Au–18Ni filler metal is significantly lower than the yield strength of the steel, whereas the difference in the tensile strength is relatively small.

In Fig. 8 the applied load on the DCB specimens is presented as a function of the CMOD for four samples. All specimens showed a very similar behaviour. The load increases linearly with increasing CMOD until local instabilities ('pop-ins') occurred between 9.2 and 10 kN. The load at which the first pop-in could be detected was used for the calculation of the critical stress intensity, K_{Ic} , according to Eq. (1a). A value of $49.0 \pm 1.7 \text{ MPa m}^{0.5}$ was determined. Fig. 9 shows the corresponding crack growth resistance curves. It can be clearly seen that with increasing crack length the fracture toughness remains almost constant at values of approximately $50 \text{ MPa m}^{0.5}$. This value is in good agreement with the value for pure gold, which is reported to be in the range between 40 and $90 \text{ MPa m}^{0.5}$ [15].

4.2. Defect assessment of brazed steel T-joints

In Tables 2 and 3, the numerically and experimentally determined fracture loads of the different T-joint specimens are compared. As could be expected, the defect containing specimens showed significantly lower fracture loads than the defect

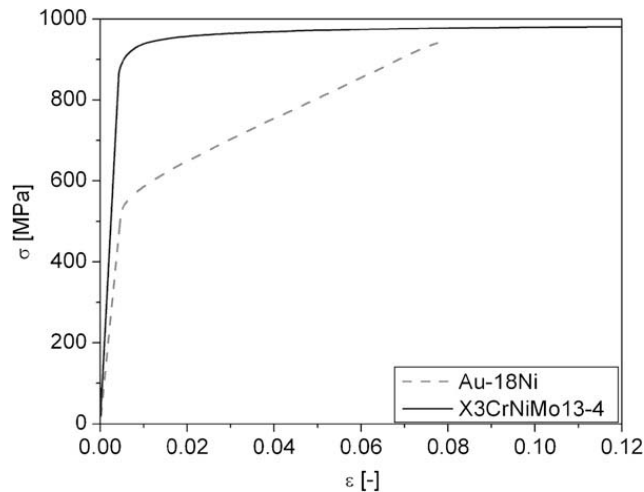


Fig. 7. Stress–strain curves of base material and filler metal derived from in situ tensile tests and inverse numerical parameter determination (Au–18Ni) and from standard tensile tests (X3CrNiMo13–4).

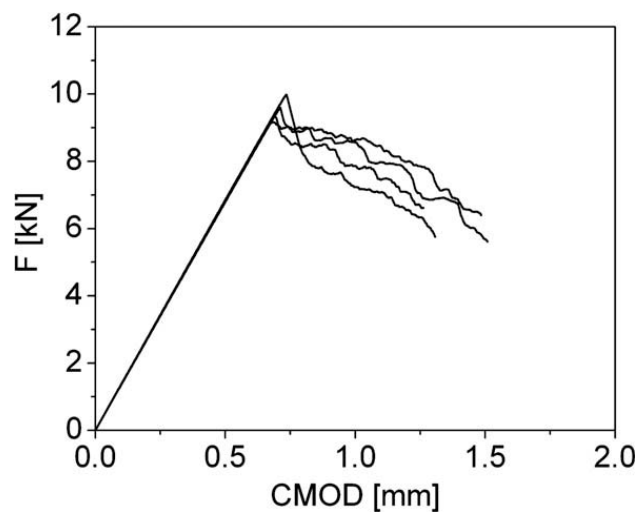


Fig. 8. Load-CMOD curves taken from DCB-specimens.

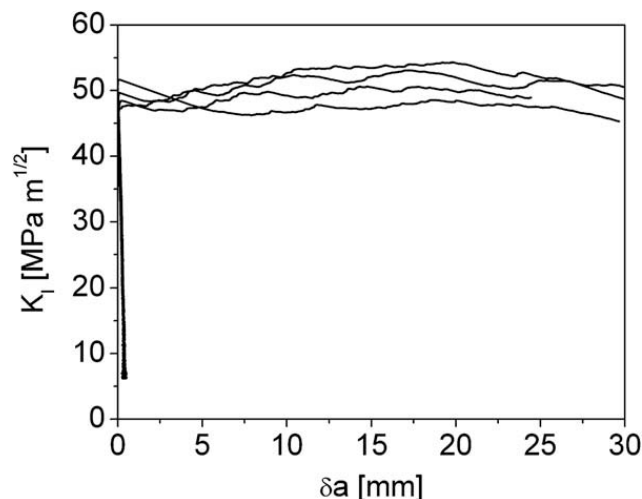


Fig. 9. Crack growth resistance curves taken from DCB-specimens.

Table 2

Numerically ($F_{max,FE}$) and experimentally ($F_{max,exp}$) determined limit loads for T-joint specimens containing straight defects.

Defect size a (mm)	0	0.5	1	2	3	4
$F_{max,FE}$ (kN)	130.6	93.6	69.4	45.0	27.0	16.1
$F_{max,exp}$ (kN)	123.3 (± 7.0)	–	–	33.1 (± 18.0)	–	18.6 (± 3.6)

free reference specimens. For the straight defects, a remarkable correlation between the two for the maximum load was obtained. A considerably lower load was measured in the tensile tests only for one specimen. For the semi-elliptical defects, a good agreement between numerical and analytical results was achieved for defects with $a > 2.5$ mm. For a defect size of 3 mm, the experimental value is almost equal to the predicted one.

The fracture behaviour of the T-joints was characterized by stereomicroscopy as well as by SEM. In Fig. 10a, the fracture surface of a T-joint specimen with an elliptical defect is shown as an example. It can be clearly seen that the specimen fractured in the brazing zone, and not as a result of delamination along the steel–filler metal interface. A stepped fracture pattern was observed on the fracture surfaces, which is also evident at a higher magnification in the SEM (Fig. 10b). In addition ductile deformation features containing ductile dimples could be observed on the fracture surface (Fig. 10c). This shows that the specimens fracture in a microscopically ductile way, even if the results of the fracture toughness measurements suggest a macroscopically brittle fracture behaviour. This can be related to the small thickness of the Au–18Ni interlayer of approx. 100 μm . Even if the layer is plastically deformed to 6%, the overall elongation is very small.

In the case of the specimen showing a significantly lower load than predicted, a subsequent examination of the fracture surfaces revealed that the filler metal delaminated from the steel in the vicinity of the defect edge, which has not been taken into account in the FE simulations.

In order to compare the experimental and the numerical results with the predictions of the standard failure assessment procedure according [8], a set of failure assessment diagrams (FAD) was constructed. In contrast to the FAD in [8], which present the normalized stress intensity K_r as a function of the normalized load L_r and a limit curve according to Eqs. (2) and (3)

$$\text{with } K_r = \frac{K_I}{K_{Ic}} \quad \text{and} \quad L_r = \frac{\sigma_{max}}{UTS} = \frac{F_{max}}{A \cdot UTS}$$

where K_I is the local stress intensity, K_{Ic} is the critical stress intensity factor, σ_{max} and F_{max} are the maximal applicable nominal stress and maximal applicable load, respectively, applied to the component, A is the cross sectional area of the T-joint and UTS the ultimate tensile strength according to Table 1, the FADs suggested in this work give directly the maximal applicable load F_{max} as a function of the defect size a . K_I is a function of the geometry and the size of the defect as well as of the specimen geometry and the applied load. In our work, the ultimate tensile strength was used for calculating L_r instead of the yield strength since it is much easier to determine for brazed specimens. The K_I values as a function of the applied load for the specimens and defects investigated in this work were derived in [16]. Any other relevant parameter was determined in this work. The results were further compared with the theoretical limit load which only takes into account the reduction of the cross section in the brazing zone due to the defects, but not the corresponding stress concentrations. The theoretical limit loads for the specimens and defects investigated in this work were determined in [16].

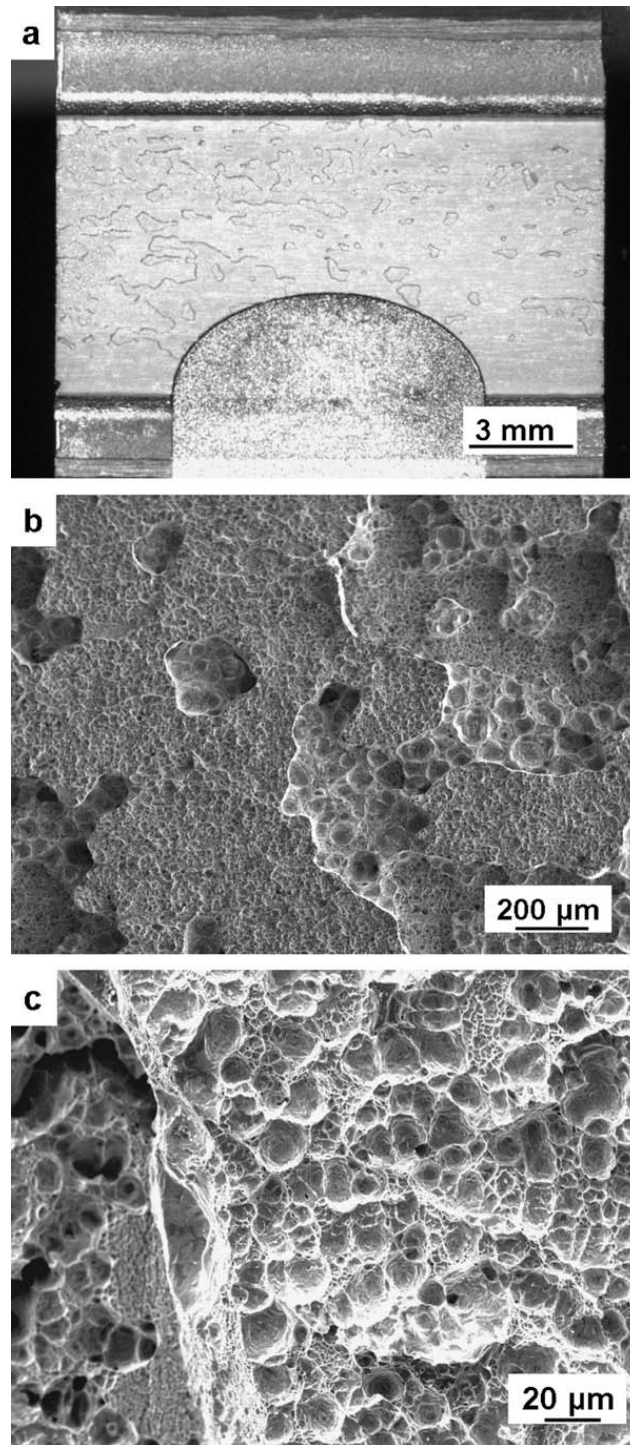


Fig. 10. Stereo microscope (a), and SEM images (b,c) of fracture surfaces.

Fig. 11 shows the FADs for the straight (a) and the semi-elliptical (b) defects. Besides the results from the tensile tests (\blacktriangle) and the data obtained from the FE calculations (\blacksquare), the theoretical load (—) is presented. The results are compared with the maximum loads obtained from the procedure according to R6, option 1 (\bullet).

The experimental and numerical results correlate well with the predictions according to the R6 procedure. However, all values deviate strongly from the theoretical limit load. This clearly shows that the stress concentrations at brazing defects must be taken into account for calculating the strength of defect containing brazed components. For smaller defects of both types (straight: $a < 1$ mm, semi-elliptical: $a < 2$ mm) the values obtained from the FE simulations are generally higher than those predicted by the R6 procedure. This might be a result of the pronounced multiaxial stresses in the filler metal, which enables stresses exceeding the tensile strength to be present in the filler metal [5]. For larger defects, a nearly perfect correlation between the experiments and the calculations was found. This shows that this failure assessment procedure

Table 3

Numerically ($F_{\max,FE}$) and experimentally ($F_{\max,exp}$) determined limit loads for T-joint specimens containing semi-elliptical defects.

Defect size a (mm)	0	1.5	3	4
$F_{\max,FE}$ (kN)	130.6	85.8	56.3	51.2
$F_{\max,exp}$ (kN)	123.3 (± 7.0)	–	42.5 (± 11.3)	–

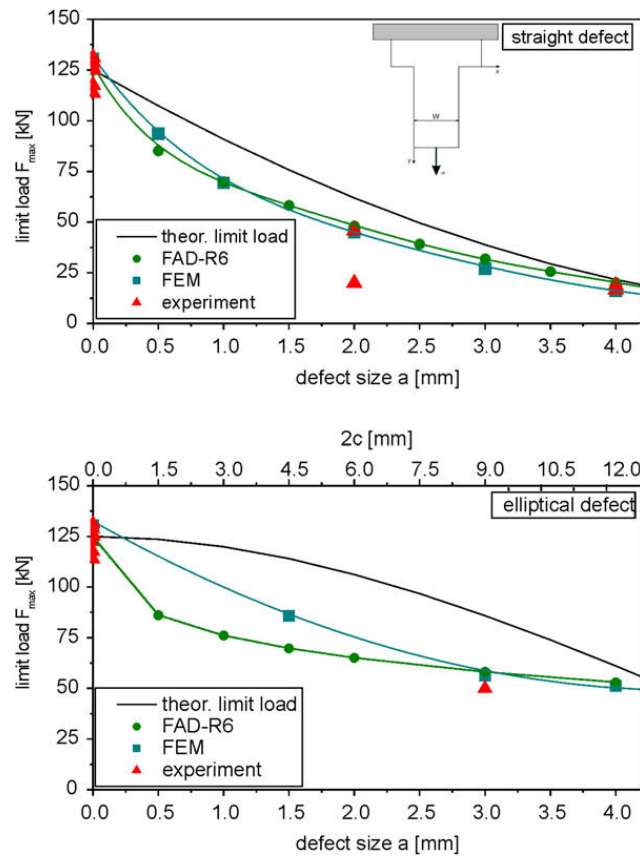


Fig. 11. Failure assessment diagrams – comparison between experimental, numerical and analytical results: (a) straight defects, (b) semi-elliptical defects.

can be used for estimating the damage tolerance of brazed components. However, the procedure accounts only for defects arising from incomplete gap filling, and a possible interaction of different neighbouring defects such as pores or microcracks in the brazing zone is not taken into account.

5. Summary

In this work, the mechanical performance together with the defect tolerance of high temperature brazed steel joints were investigated both theoretically and experimentally. Besides mechanical tests for determining the strength or the fracture toughness, tensile tests on specimens with T-joint geometry containing crack-like defects were performed.

The experimental results were compared with numerical results from 3D FE simulations as well as with analytical results obtained from the standard R6 procedure. A remarkable agreement between the experiments and the calculations was found. This shows that the FAD approach as suggested in the R6 procedure can be applied for the engineering defect assessment of brazed components.

Acknowledgements

The present work was financially supported by MAN Turbo AG, Zurich. The authors would like to thank Dr. H. Gut.

References

[1] Nowacki J, Swider P. Producibility of brazed high-dimension centrifugal compressor impellers. *J Mater Process Technol* 2003;133:174–80.
 [2] Wu XW, Chandel RS, Seow HP, Li H. Brazing of Inconel X-750 to stainless steel 304 using induction process. *Mater Sci Eng A* 2000;288:84–90.
 [3] Shiue RK, Wu SK, Chen SY. Infrared brazing of TiAl intermetallic using BAg-8 braze alloy. *Acta Mater* 2003;51:1991–2004.

- [4] American National Standard AWS C3.6M/C3.6:2008. Specification for furnace brazing. American Welding Society; 2007.
- [5] Kassner ME, Kennedy TC, Schrems KK. The mechanism of ductile fracture in constrained thin silver film. *Acta Mater* 1998;46(18):6445–57.
- [6] Tolle MC, Kassner ME, Cerri E, Rosen RS. Mechanical behaviour and microstructure of Au–Ni brazes. *Metall Mater Trans A* 1995;26A:941–8.
- [7] Varias AG, Suo Z, Shih CF. Ductile failure of a constrained metal foil. *J Mech Phys Solids* 1991;39(7):963–86.
- [8] British Energy Generation Ltd. R6-Rev. 4; 2002.
- [9] BS 7910:1999. Guide on methods for assessing the acceptability of flaws in metallic structure. BSI; 2000.
- [10] Webster S, Bannister A. Structural integrity assessment procedure for Europe – of the SINTAP programme overview. *Eng Fract Mech* 2000;67:481–514.
- [11] Kim YJ, Koçak M, Ainsworth RA, Zerbst U. SINTAP defect assessment procedure for strength mismatched structures. *Eng Fract Mech* 2000;67:529–46.
- [12] Lehmann H, Schindler HJ. EMPA-Swiss Federal Institute for Materials Testing and Research. Report No. 203'305-041122; 2004.
- [13] Cugnoni J, Botsis J, Janczak-Rusch J. Size and constraining effects in lead-free solder joints. *Adv Eng Mater* 2006;8(3):184–91.
- [14] Belytschko T, Bindeman LP. Assumed strain stabilization of the 8 node hexahedral element. *Comput Meth Appl Mech Eng* 1993;105:225–60.
- [15] CES Selector. Version 4.6.1. Granta Design Limited.
- [16] Leinenbach C, Lehmann H, Schindler HJ. *MP Mater Test* 2007;4:149–56.